The Astrophysical Journal, 971:74 (12pp), 2024 August 10 https://doi.org/10.3847/1538-4357/ad5cef

Investigating Optical Variability of the Blazar S5 0716+714 on Diverse Timescales

Ergün Ege[1], Aykut Özdönmez[2], Aditi Agarwal[3], and Tansel Ak[4]
[1] Istanbul University, Institute of Graduate Studies in Science, 34116, Beyazit, Istanbul, Turkey
[2] Ataturk University, Faculty of Science, Department of Astronomy and Space Science, 25240, Yakutiye, Erzurum, Turkey
[3] Center for Cosmology and Science Popularization (CCSP) SGT University, Budhera, Delhi- NCR—122006, India
[4] Istanbul University, Faculty of Science, Department of Astronomy and Space Sciences, 34116, Beyazıt, Istanbul, Turkey
Received 2024 March 19; revised 2024 June 5; accepted 2024 June 17; published 2024 August 7

Abstract

We present the results of the observational study of the blazar S5 0716+716 in the optical bands *B*, *V*, *R*, and *I* between 2019 March and 2023 August to investigate its variability on diverse timescales. The blazar was followed up by the T60 robotic telescope in Türkiye for 416 nights to obtain long-term variability during this period. In order to search for the intraday variability of the object, we have carried out 21 nights of observations with the T100 telescope for at least 1 hr. The blazar showed a ∼2.47 mag variation in the optical *R* band during our monitoring period, the brightest state on 2020 January 18 (MJD 58866) as $R = 12.109 \pm 0.011$ mag and the faintest state on 2019 March 23 (MJD 58565) as $R = 14.580 \pm 0.013$ mag. We employed the nested ANOVA test and the power-enhanced F-test to quantify intraday variability, which showed that the blazar was significantly variable in the *R* band on 12 out of 21 nights. Correlation analysis of the light curves shows that the emission in the *BVRI* optical bands was strongly correlated both in the short and long term without any time lag. The blazar has likely quasiperiods of 186 ± 30 and 532 ± 76 days in the optical *R*-band light curve according to the weighted wavelet Z-transform and Lomb–Scargle periodogram. The intraday variation and long-term variation features are discussed within the frame of prospective scenarios.

Unified Astronomy Thesaurus concepts: BL Lacertae objects (158); Blazars (164); Active galactic nuclei (16)

Materials only available in the online version of record: data behind figure, machine-readable tables

1. Introduction

The blazar class of active galactic nuclei (AGNs) is comprised of BL Lacertae (BL Lac) objects and flat spectrum radio quasars (FSRQ). These objects are characterized by having rapid and high flux variability across the entire electromagnetic spectrum, from radio to gamma-rays, as well as strong optical polarization. In particular, the BL Lac subclass is notable for its weak or lack of line profile in the optical spectra (Urry & Padovani 1995; Wagner & Witzel 1995). Having relativistic jets pointing close to the observer's line of sight ($<10°$) makes their nonthermal radiation dominant (Krawczynski 2004). Like the other AGNs, the broadband continuum of the spectral energy distribution (SED) of blazars has two humps. The low energy part, from radio to X-ray, is synchrotron emission produced by relativistic electrons in the jet, the high energy part, from X-ray to γ-ray, is inverse Compton emission explained by various models; leptonic, hadronic, or a lepto-hadronic mixture (Romero et al. 2017).

The variability of blazars is classified based on the timescale of the flux variations. Intraday variation (IDV) or micro-variation refers to the variations in the flux of up to a few tenths of a magnitude that occur over a timescale of a few minutes to a day (Wagner & Witzel 1995). Short-term variation (STV) refers to variabilities that are greater than 1 magnitude and occur over a period of several months. Long-term variation (LTV) refers to changes in the flux of several magnitudes over a timescale of months to many years (Massaro et al. 2001; Gupta et al. 2008a).

The timescales of the variability are associated with different radiation processes. Several scenarios have been proposed to explain the observed flux variations in blazars: instabilities in the accretion disk (Wiita 1996), the precession of the jet (Kudryavtseva et al. 2011), shocks moving through the jet (Marscher & Travis 1996), and changes in the Doppler factor due to relativistic emission plasma following a spiral path in the jet (Raiteri et al. 2017), etc. The color change that accompanies the flux variation can lead to an elaboration of the structure of the source (Villata et al. 2002; Agarwal et al. 2016). The analysis of flux variations and spectral behavior provides insights into the dynamics and timescales of electron cooling in the blazar jets as well as facilitates the testing of theoretical models (Raiteri et al. 2003; Gupta et al. 2008b). Finding a trace of any periodicity in the flux variation provides clues about the accretion disk and central region, the SMBH, and the jet (Schmidt et al. 2011; Chatterjee et al. 2018; Otero-Santos et al. 2020).

S5 0716+714 ($\alpha = 07\mathrm{h}21\mathrm{m}53\overset{s}{.}44$, $\delta = +71°20'36\overset{''}{.}4$) is one of the brightest BL Lac objects in the optical bands (Rani et al. 2013), and located at a distance of $z = 0.2304 \pm 0.0013$ (Pichel et al. 2023). It was first discovered in a 5 GHz survey of extragalactic radio sources in 1979 (Kuehr et al. 1981). It was detected in the very high energy (>100 GeV) γ-ray band by the MAGIC telescope during an optical flare in 2008 (Anderhub et al. 2009). BL Lac objects are classified as low synchrotron peaked blazars ($\nu_{\rm peak} \leqslant 10^{14}$ Hz), intermediate synchrotron peaked blazars (IBL; 10^{14} Hz $\leqslant \nu_{\rm peak} \leqslant 10^{15}$ Hz), and high synchrotron peaked blazars ($\nu_{\rm peak} \geqslant 10^{15}$ Hz) according to the peak frequency of the synchrotron hump (Abdo et al. 2010). The blazar has a luminosity of 10^{46} erg s^{-1} and a peak in the UV X-ray band at a frequency of $10^{14.96}$ Hz (Fan et al. 2016), which places it in the IBL class of blazars.

Its brightness and extreme variability make it a popular target for multiwavelength observations and time-domain astrophysical studies (e.g., Wagner et al. 1996; Ostorero et al. 2006; Gupta et al. 2012; Liao et al. 2014; Chandra et al. 2015; Dai et al. 2015). The blazar had a brightness of 11.6 mag (optical R band), which is the brightest value ever recorded on during its flare state (Agarwal et al. 2016). The blazar was historically observed in its faintest state on 2014 January 6 ($R = 14.85 \pm 0.06$ mag) by Kaur et al. (2018). Several studies have suggested different quasiperiodic oscillations (QPOs) in the optical bands. Hong et al. (2018) detected a QPO of 50 minutes. Haiyan et al. (2023) detected a QPO of 2.90 ± 0.14 yr using 32 yr of optical R-band data and associated the QPO with a probable binary SMBH. Chen et al. (2022) detected a transient QPO of 31.3 ± 1.8 days in the γ-ray band light curve (LC) of the blazar S5 0716+714 using weighted wavelet Z-transform (WWZ) and Lomb–Scargle periodogram (LSP). Likely QPOs of 24.24 ± 1.09 days, 24.12 ± 0.76 days, and 24.82 ± 0.73 days in the optical V, R, and I bands, respectively, were identified by Yuan et al. (2017). In the optical and radio data of S5 0716+714, Raiteri et al. (2003) detected a periodicity of 3.0 ± 0.3 yr and a 5.5–6 yr, respectively. This result is very close to that of Li et al. (2023), which is 2.63 ± 0.22 yr in γ-ray. Using the autocorrelation function analysis, Liao et al. (2014) identified variability timescales of ∼60–90 days across 14.5 GHz radio, optical V, X-ray, and γ-ray LCs and γ-ray and optical bands are found to be correlated during the flares. Bhatta et al. (2013) obtained a 72 hr continuous optical LC with WEBT in 2009 February, which showed no periodicity.

The spectral behavior of the blazar S5 0716+714 has been studied by many researchers. Some studies have claimed that the source has the property of being bluer when it is brighter (bluer when brighter, BWB), both on short- and long-term timescales (Ghisellini et al. 1997; Villata et al. 2008; Chandra et al. 2011; Agarwal et al. 2016; Bhatta et al. 2016; Hong et al. 2017; Gorbachev et al. 2022) while others have found the opposite (Stalin et al. 2006; Volvach et al. 2012) or monitored either (Raiteri et al. 2003).

In this paper, we present the comprehensive variability results of the optical observational study of the blazar S5 0716+714 on diverse timescales. The paper is structured as follows: Section 2 provides brief information of the observations, the telescopes used, and the data reduction process. Section 3 describes the statistical analysis techniques used to quantify the variability, investigate the correlations, and detect the periodicity. The results obtained are presented in Section 4. The results are discussed and conclusions are drawn in Section 5.

2. Observations and Data Reduction

The photometric observations of S5 0716+714 were carried out in the optical *BVRI* bands with two optical telescopes T60 and T100 at the campus of the National Observatory of Türkiye located in Bakirlitepe, Antalya, Türkiye. The T100 telescope has a 1 m mirror and it is equipped with a cryogenic-cooled CCD (model SI 1100 Cryo, size 4096 × 4037 px). The T60 is a robotic telescope with a 60 cm mirror and a thermally cooled CCD (model Andor iKon-L, size 2048 × 2048 px).

The observation period for the T100 and T60 telescopes was between 2019 March and 2023 August. The T100 telescope was used to collect data for IDV analysis, allocating at least 1 hr and more in each observation night, while the T60 robotic telescope followed the target by taking at least two frames in each optical band filter as many nights as possible, depending on the weather conditions. Exposure times range from 2 to 120 s and 15 to 120 s with the T100 and T60 telescopes respectively, depending on the filter, and the brightness of the blazar.

Calibration of the raw images taken by the T100 telescope was done using standard Python libraries (e.g., astropy and ccdproc) using bias and flat frames taken regularly by the observatory's technical staff. Since the CCD detector on the T100 telescope is cooled up to −95°C, no dark calibration was performed on the frames taken by the T100. The bias, dark, and flat fielding calibrations of the frames taken by the T60 robotic telescope were performed by the observatory pipeline. To obtain the instrumental magnitudes of the S5 0716+714 and the standard comparison stars, aperture photometry was performed on the nightly frames within aperture radii between 1 × FWHM and 5 × FWHM to obtain the best signal-to-noise ratio. The finding chart of the blazar is taken from the study of Villata et al. (1998) and the brightnesses of the standard stars are taken from Ghisellini et al. (1997) and Villata et al. (1998). We provide our observational data, including instrumental magnitudes, exposure times, and dates, in the online data. We have taken into account magnitudes with an error less than 0.1 mag resulting in a data set with an average error of 0.051 mag. We have used star S5 as a reference, and stars S3 and S6 as comparisons for the evaluation of the blazar's flux, because of their high signal-to-noise ratio, close position to the source, close magnitude, and comparable color characteristics, which mitigate possible discrepancies in the photon statistics of the photometric measurements. The flux values are reliable because the target and the standard stars are very close together in the same field of view, i.e., have the same air mass and measurement conditions. After applying the galactic extinctions given in the NASA Extragalactic Database[5] as $A_B = 0.112$, $A_V = 0.085$, $A_R = 0.067$, and $A_I = 0.047$ (Schlafly & Finkbeiner 2011), the resulting magnitudes were converted to the corresponding fluxes following Bessell et al. (1998).

3. IDV

3.1. Flux Variability

To study the flux variability of blazars at different frequencies is essential to delineate both the size and the structure of the emission regions and the radiative process. Only those nights with more than 1 hr of observations were analyzed to ensure that there were enough data points to detect meaningful IDV. We have 21 nightly observations that meet this criterion, of which 6 are multiband (BVRI) and 15 are R band only. The LCs of these 21 night observations are shown in Figure 1.

Various statistical methods have been used to quantitatively characterize variable sources, depending on the data to be analyzed. To reveal the variability characteristics of the blazar in the optical *BVRI* bands on the intraday timescale, we used the most common and robust statistical techniques; i.e., the power-enhanced F-test and the nested ANOVA test.

The power-enhanced F-test is a tool for comparing the blazar LC with the combined variance of the comparison stars, which has been used in recent studies to detect IDV quantitatively (e.g., Gaur et al. 2015; Poledniková et al. 2016; Pandey et al. 2019;

[5] https://ned.ipac.caltech.edu

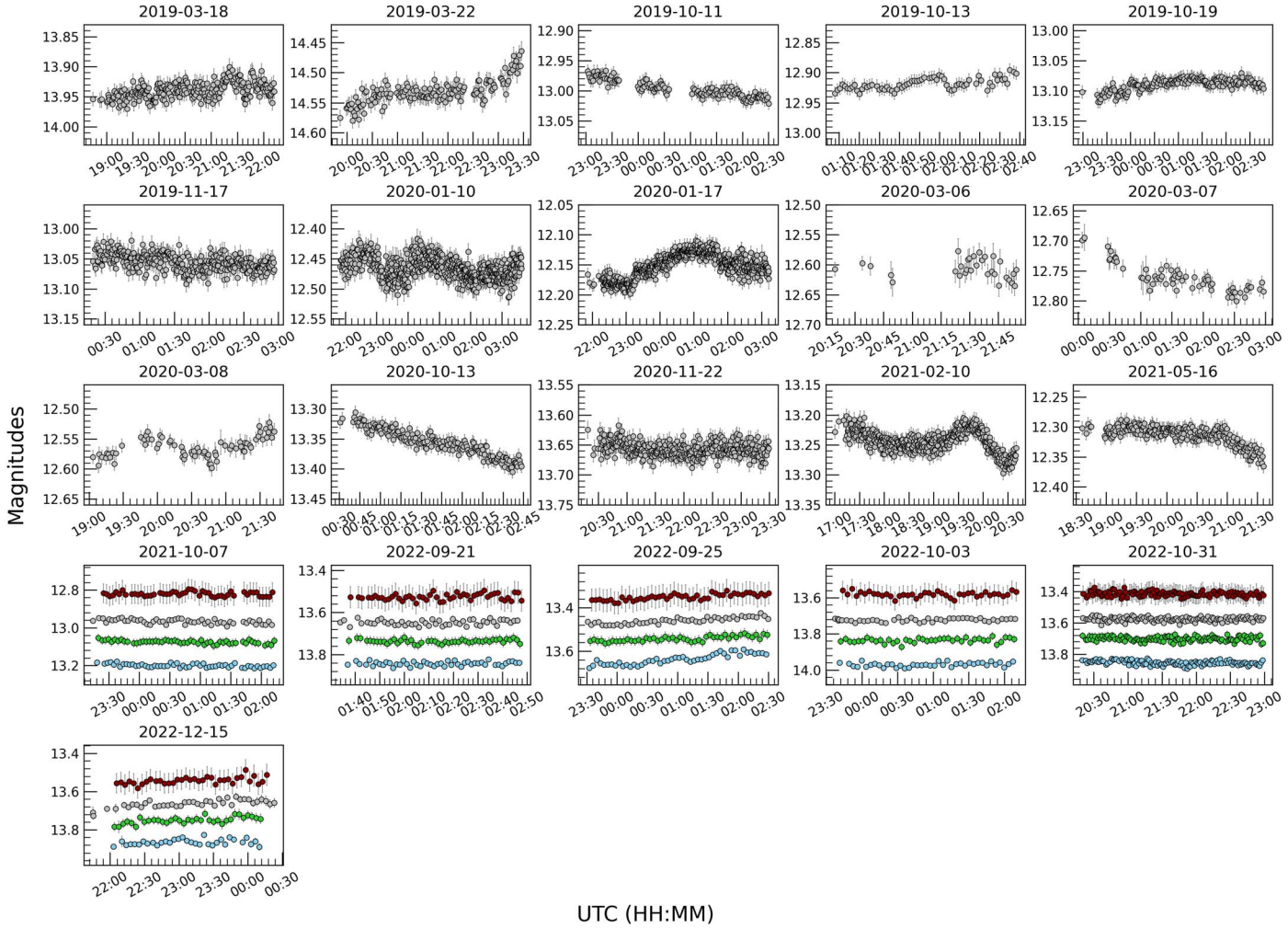

Figure 1. Intraday LCs of the blazar S5 0716+714 in the optical *BVRI* − bands. For better visualization, the dark red, silver, green, and blue circles represent the *B*-, *V*-, *R*-, and *I*-band magnitudes with an offset of −0.6, −0.28, 0.0, and +0.35, respectively. The dates of the observations are given at the top of each plot. The complete observational log and results in the *B*, *V*, *R*, and *I* bands are available as the data behind the figure.

(The data used to create this figure are available in the online article.)

Agarwal et al. 2022). The power-enhanced F-statistic is defined as:

$$F_{\rm enh} = \frac{s^2_{\rm blz}}{s^2_c}, \tag{1}$$

where $s^2_{\rm blz}$ is the estimated variance difference between the blazar and the reference star, and $s^2_{\rm c}$ represents the combined variance of the comparison star and the reference star calculated with Equation (13) in de Diego (2014).

In our research, we have used the field star S5 as a reference star, which is the reference star with the closest magnitude to the blazar. The field stars S3 and S6 are used as comparison stars ($k = 2$). Since the comparison stars and the blazar are in the same field, we have the same number of observations for each (N), the F-statistics have $\mu_1 = N - 1$ and $\nu_2 = k(N - 1)$ degrees of freedom (DOF) in numerator and denominator, respectively. We have estimated the $F_{\rm enh}$ and compared it with the critical value (F_c) at $\alpha = 0.01$, corresponding to a 99% confidence level. An LC is classified as variable (V) if $F_{\rm enh} \geqslant F_c$, and otherwise as nonvariable (NV).

The ANOVA (for Analysis of Variance) is a tool for evaluating the mean values of the dispersion between groups of observations. The Nested ANOVA is a modified version of ANOVA that allows the use of multiple reference stars to generate differential LCs of the blazar. Since the nested ANOVA does not require a comparison star, all reference stars are used in the test. In our study, we used three reference stars (S3, S5, and S6) to generate differential LCs of the blazar. The differential LCs are divided into groups of five points each. The mean square due to the groups ($\rm MS_G$) and the nested observations in the groups ($\rm MS_{O_G}$) were calculated according to Equation (4) from de Diego et al. (2015; see also Montgomery 2012, Chapter 14).

The resulting ratio $F = \rm MS_G/MS_{O_G}$ corresponds to an F-distribution with $(a - 1)$ and $(a(b - 1))$ DOF, in the numerator and denominator, respectively. For a significance level of $\alpha = 0.01$, the LC is classified as V if the F-statistic is greater than or equal to the critical value (F_c), otherwise, it is NV.

To quantify the variability amplitude, we used the following equation,

$$A = 100 \times \sqrt{(A_{\rm max} - A_{\rm min})^2 - 2\sigma^2}\ [\%], \tag{2}$$

where $A_{\rm max}$ and $A_{\rm min}$ are the maximum and the minimum values of the measured magnitudes over the entire observation period, and σ is the mean error (Heidt & Wagner 1996).

Table 1
The Test Results of IDV of the Blazar S5 0716+714

Obs. Date yyyy-mm-dd	Band	Avg. Mag.	t_{obs} (hr)	Power-enhanced F-test			Nested ANOVA Test			Status	Amplitude (%)
				DOF(ν_1,ν_2)	F_{enh}	F_c	DOF(ν_1,ν_2)	F	F_c		
2019-03-18	*R*	13.939	3.46	(239, 478)	0.54	1.29	(47, 192)	5.00	1.65	NV	...
2019-03-22	*R*	14.531	3.60	(140, 140)	2.45	1.48	(27, 112)	12.65	1.91	V	11.23
2019-10-11	*R*	12.997	3.48	(130, 130)	5.39	1.51	(25, 104)	52.39	1.96	V	5.10
2019-10-13	*R*	12.919	1.50	(67, 67)	3.02	1.78	(12, 52)	12.00	2.55	V	3.73
2019-10-19	*R*	13.090	3.80	(169, 338)	0.08	1.35	(33, 136)	32.24	1.81	NV	...
2019-11-17	*R*	13.055	2.62	(319, 638)	1.59	1.25	(63, 256)	5.44	1.55	V	7.01
2020-01-10	*R*	12.466	5.80	(606, 1212)	1.28	1.18	(120, 484)	7.78	1.38	V	9.41
2020-01-17	*R*	12.151	5.35	(598, 1196)	4.63	1.18	(118, 476)	52.52	1.38	V	8.40
2020-03-06	*R*	12.607	1.58	(30, 60)	1.10	2.03	(5, 24)	4.80	3.90	NV	...
2020-03-07	*R*	12.762	2.90	(64, 128)	3.84	1.63	(12, 52)	26.54	2.55	V	10.08
2020-03-08	*R*	12.564	2.66	(71, 142)	3.12	1.59	(13, 56)	19.67	2.47	V	7.20
2020-10-13	*R*	13.356	2.21	(168, 336)	5.92	1.36	(32, 132)	72.12	1.82	V	9.41
2020-11-22	*R*	13.657	3.18	(366, 732)	0.77	1.23	(72, 292)	2.54	1.51	NV	...
2021-02-10	*R*	13.244	3.66	(430, 860)	2.96	1.21	(85, 344)	21.32	1.46	V	9.19
2021-05-16	*R*	12.314	3.00	(209, 418)	2.64	1.31	(41, 168)	39.22	1.71	V	7.46
2021-10-07	*B*	13.800	2.89	(53, 106)	1.27	1.71	(9, 40)	4.06	2.89	NV	...
2021-10-07	*V*	13.355	2.89	(52, 104)	0.95	1.72	(9, 40)	6.72	2.89	NV	...
2021-10-07	*R*	12.966	2.94	(53, 106)	1.50	1.71	(9, 40)	5.08	2.89	NV	...
2021-10-07	*I*	12.470	2.77	(49, 98)	0.74	1.74	(9, 40)	4.80	2.89	NV	...
2022-09-21	*B*	14.443	1.17	(47, 94)	0.73	1.76	(8, 36)	0.74	3.05	NV	...
2022-09-21	*V*	14.016	1.16	(47, 94)	0.67	1.76	(8, 36)	2.92	3.05	NV	...
2022-09-21	*R*	13.647	1.20	(49, 98)	0.80	1.74	(9, 40)	1.89	2.89	NV	...
2022-09-21	*I*	13.176	1.16	(48, 96)	0.96	1.75	(8, 36)	0.70	3.05	NV	...
2022-09-25	*B*	14.237	2.92	(47, 94)	3.94	1.76	(8, 36)	43.68	3.05	V	7.88
2022-09-25	*V*	13.822	2.92	(47, 94)	1.94	1.76	(8, 36)	17.69	3.05	V	4.41
2022-09-25	*R*	13.459	2.98	(48, 96)	2.43	1.75	(8, 36)	22.10	3.05	V	5.57
2022-09-25	*I*	13.000	2.92	(47, 94)	2.32	1.76	(8, 36)	11.13	3.05	V	5.45
2022-10-03	*B*	14.569	2.43	(39, 78)	1.15	1.86	(7, 32)	1.22	3.26	NV	...
2022-10-03	*V*	14.115	2.43	(40, 80)	0.91	1.85	(7, 32)	1.54	3.26	NV	...
2022-10-03	*R*	13.723	2.53	(43, 86)	0.46	1.81	(7, 32)	1.67	3.26	NV	...
2022-10-03	*I*	13.231	2.43	(40, 80)	1.23	1.85	(7, 32)	1.34	3.26	NV	...
2022-10-31	*B*	14.454	2.64	(118, 236)	1.13	1.44	(22, 92)	3.96	2.04	NV	...
2022-10-31	*V*	13.981	2.64	(119, 238)	0.82	1.43	(23, 96)	1.00	2.01	NV	...
2022-10-31	*R*	13.576	2.64	(122, 244)	0.74	1.43	(23, 96)	1.73	2.01	NV	...
2022-10-31	*I*	13.065	2.64	(116, 232)	0.71	1.44	(22, 92)	1.37	2.04	NV	...
2022-12-15	*B*	14.465	2.12	(32, 64)	0.82	1.98	(5, 24)	3.82	3.90	NV	...
2022-12-15	*V*	14.030	2.12	(34, 68)	1.76	1.95	(6, 28)	4.90	3.53	NV	...
2022-12-15	*R*	13.664	2.63	(39, 78)	1.56	1.86	(7, 32)	7.06	3.26	NV	...
2022-12-15	*I*	13.193	2.18	(35, 70)	1.09	1.93	(6, 28)	3.02	3.53	NV	...

(This table is available in machine-readable form in the online article.)

Table 2
Duty Cycle of the Intraday Observations within Different Observation Durations

Band	$t_{obs} \geqslant 1$ hr		$t_{obs} \geqslant 2$ hr		$t_{obs} \geqslant 3$ hr	
	$N_{V,T}$	DC (%)	$N_{V,T}$	DC (%)	$N_{V,T}$	DC (%)
B	1, 6	12	1, 5	18	...	...
V	1, 6	12	1, 5	18	...	...
R	12, 21	52	11, 18	59	6, 9	64
I	1, 6	12	1, 5	18	...	...
For IDV with Brighter than Average LTV mag.						
R	8, 10	74	7, 8	86	4, 4	100

Note. $N_{V,T}$ is the number of variables and total nights, respectively.

Table 1 shows the results of the F_{enh}-tests and nested ANOVA tests. An LC is classified as V in the table only if significant variations were confirmed by both tests, otherwise, it is classified as NV. Variability amplitudes were also calculated for the nights showing IDV.

The source was variable on minute timescales on seven nights with a variability amplitude between 3.73 and 11.23. Although multiband LCs are available for 2022 September 25 and 2022 December 15, only one band (*B* band and *V* band, respectively) of the LC showed variability. The duty cycle (DC) is commonly used as a quantitative measure to assess the likelihood of variability of a source. The DC is defined as the fraction of nights showing variability out of the total number of nights (Romero et al. 1999),

$$\mathrm{DC} = 100\frac{\sum_{i=1}^{n}(N_i/\Delta t_i)}{\sum_{i=1}^{n}(1/\Delta t_i)}[\%], \quad (3)$$

where $\Delta t_i = \Delta t_{i,\mathrm{obs}}(1+z)^{-1}$ is the duration of monitoring from the reference frame of the source. N_i takes a value of 1 if the source is marked as IDV, otherwise it takes a value of 0. Out of 21 observation nights between 2019 March and 2023 August,

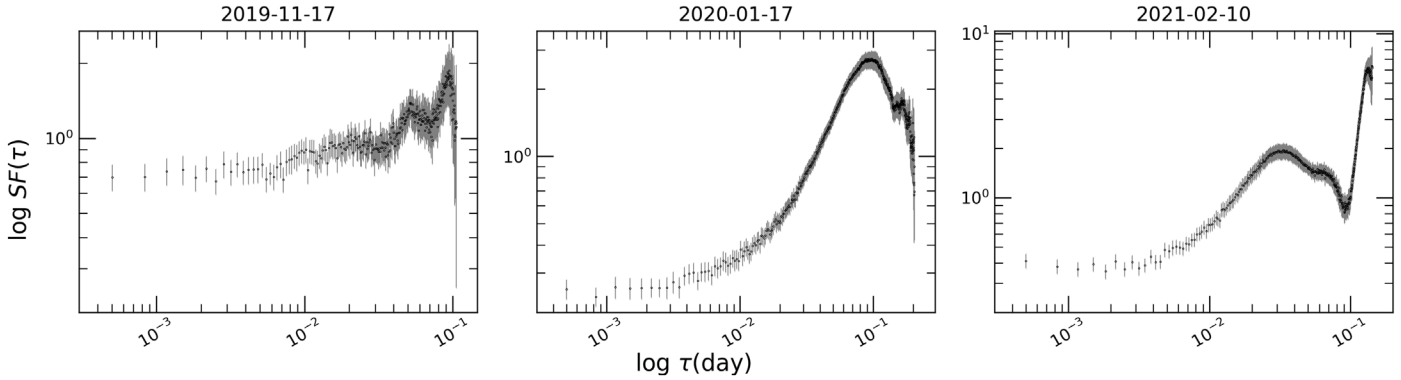

Figure 2. SF of the selected intraday LCs of the blazar S5 0716+714 in the optical R band. The dates of observation are written at the top of each plot.

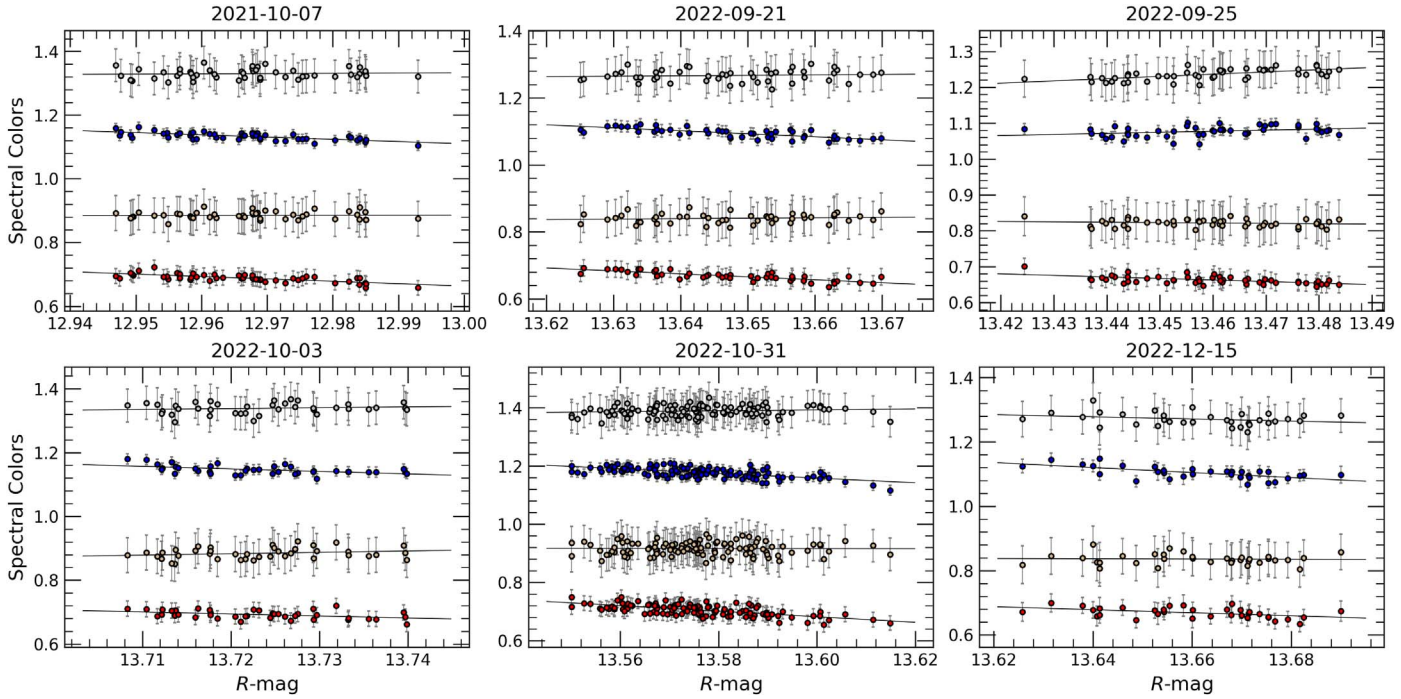

Figure 3. The intraday color–magnitude plots of the blazar S5 0716+714. The blue, silver, dark red, and light brown colored dots represent $B-R$, $B-I$, $V-R$, and $V-I$ color indices. We have added +0.3 offset values to the $B-R$ and $V-R$ colors in order to distinguish between the distributions. Black lines represent linear fits and their parameters are given in Table 3.

the blazar was monitored for at least 1, 2, and 3 hr on 21, 18, and 9 nights, respectively.

The duty cycle of IDV of the blazar S5 0716+714 has been determined in a wide range from 30% up to 100% in previous studies (Chandra et al. 2011; Agarwal et al. 2016; Kaur et al. 2018; Tripathi et al. 2024). Based on our observations, we obtained a value of up to 64% of DC in different bands and different observation durations. Hong et al. (2018) monitored the source for less than 1 hr and reported a DC of 19.57%, and, in another study carried out over 13 nights in 2012 January–February, a DC of 44% was estimated when the source was monitored for about 5 hr (Hong et al. 2017). In order to check for any correlation between the IDV of the source and the monitoring time allocated, we calculated the DC for 1, 2, or 3 hr of the monitoring period (Table 2). The results confirm the well-known fact that the longer the monitoring time, the higher the probability of detecting variability, i.e., a higher DC (Gupta & Joshi 2005; Rani et al. 2010; Hong et al. 2018). We have also calculated the DC values for the nights with magnitudes brighter than the average LTV magnitudes. The calculated DC values are dramatically increased for these nights (Table 2), suggesting IDV is related to the state of the blazar.

3.2. Minimum Timescale

The structure function (SF) is a method of indicating how much a source is variable in a given time lag (Simonetti et al. 1985) and is commonly used to quantify the timescale of variation of LCs where the data points are not evenly sampled data sets. It is a function that gives the square of the mean difference between the flux densities corresponding to the timescale. We use first-order SF, which is defined as:

$$\mathrm{SF}(\tau_i) = \frac{1}{N}\sum [M(t+\tau_i) - M(t)]^2, \quad (4)$$

where $M(t)$ is the magnitude at a given time t and τ is the time lag. Since the blazars show variability on all timescales, a typical SF graph will show a linear increase and end with a plateau (or

Table 3
Linear Fits to Colors vs. *R*-band Magnitude for IDV Data

Date	Color	m	c	r	p
2021-10-07	$B-R$	-0.70 ± 0.10	$+9.94 \pm 1.30$	-0.70	6.53e-09
	$B-I$	$+0.08 \pm 0.19$	$+0.23 \pm 2.45$	$+0.07$	6.57e-01
	$V-R$	-0.75 ± 0.10	$+10.15 \pm 1.34$	-0.72	2.41e-09
	$V-I$	$+0.02 \pm 0.15$	$+0.60 \pm 1.91$	$+0.02$	8.82e-01
2022-09-21	$B-R$	-0.89 ± 0.12	$+12.93 \pm 1.62$	-0.74	1.95e-09
	$B-I$	$+0.13 \pm 0.22$	-0.56 ± 2.95	$+0.09$	5.39e-01
	$V-R$	-0.88 ± 0.10	$+12.43 \pm 1.41$	-0.79	5.50e-11
	$V-I$	$+0.13 \pm 0.17$	-0.98 ± 2.29	$+0.12$	4.30e-01
2022-09-25	$B-R$	$+0.30 \pm 0.14$	-3.26 ± 1.86	$+0.30$	3.56e-02
	$B-I$	$+0.63 \pm 0.12$	-7.19 ± 1.59	$+0.61$	3.34e-06
	$V-R$	-0.43 ± 0.09	$+6.15 \pm 1.17$	-0.59	1.01e-05
	$V-I$	-0.10 ± 0.10	$+2.22 \pm 1.34$	-0.15	3.01e-01
2022-10-03	$B-R$	-0.79 ± 0.22	$+11.69 \pm 2.95$	-0.52	7.60e-04
	$B-I$	$+0.27 \pm 0.31$	-2.42 ± 4.31	$+0.14$	3.90e-01
	$V-R$	-0.63 ± 0.22	$+8.99 \pm 3.04$	-0.42	7.35e-03
	$V-I$	$+0.44 \pm 0.31$	-5.11 ± 4.25	$+0.22$	1.67e-01
2022-10-31	$B-R$	-0.81 ± 0.10	$+11.82 \pm 1.30$	-0.61	1.15e-13
	$B-I$	$+0.15 \pm 0.12$	-0.66 ± 1.68	$+0.12$	2.24e-01
	$V-R$	-0.95 ± 0.10	$+13.33 \pm 1.37$	-0.66	4.12e-16
	$V-I$	-0.02 ± 0.15	$+1.13 \pm 2.07$	-0.01	9.18e-01
2022-12-15	$B-R$	-0.78 ± 0.17	$+11.41 \pm 2.28$	-0.64	5.75e-05
	$B-I$	-0.33 ± 0.22	$+5.81 \pm 3.04$	-0.26	1.46e-01
	$V-R$	-0.47 ± 0.16	$+6.80 \pm 2.15$	-0.47	5.39e-03
	$V-I$	-0.05 ± 0.18	$+1.49 \pm 2.52$	-0.05	7.97e-01

saturation) unless there is no periodicity, flare, or flicker. Local minima following local maxima may indicate a repeating pattern, and the time between dips gives the periodicity. If SF has no plateau at the end, the maximum timescale of variability is longer than the monitoring time. On the other hand, a local minimum following a dip gives a minimum timescale as seen in Figure 2, and this finding can be used to place a minimum limit on the radiative size and mass of the SMBH. We obtained the SF of the nightly observations using the code described in Gallo et al. (2018) and the SF plots of the days with the most significant variations. On 2021 February 10, SF reaches to a local maximum at 0.0333 ± 0.0035 day ($\sim$48 minutes) and then has a dip after another rapid rise. On 2021 January 17 SF reaches to 0.0982 ± 0.0018 ($\sim$141 minutes) and then declines. On 2019 November 17 there is more than one local maximum and dip, which can be interpreted as flickering.

Using the minimum timescale of an accreting black hole (Elliot & Shapiro 1974), we can derive the limit of the emission region using the equation,

$$R \leq \frac{\delta c \Delta t_{\rm var}}{1+z}, \tag{5}$$

where δ is the Doppler factor, c is the speed of light, Δt is the minimum timescale, and z is the redshift of the blazar, which is 0.2304, considering that the Doppler factor δ has been taken to be between 4 and 15 in the previous studies. Assuming δ to be 15, the maximum size of the emission region can be estimated to be of the order of $\approx 10^{15}$ cm. The minimum timescale of the variability has been used to estimate the mass of the central SMBH of the blazar in numerous studies (Gupta et al. 2008b; Rani et al. 2010; Chandra et al. 2011; Dai et al. 2015; Agarwal et al. 2016; Kaur et al. 2018) by using the following equation in the study of Abramowicz & Nobili (1982) as below:

$$M = 1.62 \times 10^4 \frac{\delta \Delta t}{1+z} M_{\odot}. \tag{6}$$

Assuming δ is 15, the mass of the SMBH is estimated to be $5.69 \times 10^8 M_{\odot}$ (assuming the SMBH is a Kerr black hole).

3.3. Spectral Variability

Optical flux variations of blazars are often associated with spectral changes. To investigate the spectral variability of the blazar S5 0716+714 on intranight timescales, we have plotted the spectral colors against the *R*-band magnitude for each night. An example is shown in Figure 3. For the configuration of the spectral colors, we have chosen the color indices $B-R$, $B-I$, $V-R$, and $V-I$ with the larger frequency base. In order to quantitatively determine the correlation between the spectral colors and brightness, we performed a regression analysis by fitting a straight line, using the linear model $y = mx + c$ ($y =$ color index, $x =$ mean magnitude), and extracted the parameters slope (m), intercept (c), correlation coefficient (r), and p-value given in Table 3. We could not find a strong color relation so the blazar shows an achromatic behavior on the intraday scale. We should note that our multiband night observations were made when the blazar was in a relatively quiescent state.

4. LTV

4.1. Flux Variability

The blazar S5 0716+714 was simultaneously followed up in the optical *BVRI* bands for 416 nights between 2019 March and 2023 August. The resulting long-term LC can be seen in Figure 4. The brightness of the blazar in the optical *R* band has varied between 12.109 ± 0.011 (on MJD 58866) and 14.580 ± 0.013 (on MJD 58565). The mean magnitude was 13.080 ± 0.012 and the variability amplitude was 247.043%. The brightness in the *BVRI* bands is summarized in Table 4. Considering the known periodicity and the historical brightness, we observed the object in both high and quiescent states. The blazar showed a near-infrared brightening in 2019 December (Carrasco et al. 2019) before we detected the highest state of our monitoring period on 2020 January 18. From early 2022 onwards, the source is likely to be in its quiescent phase, fainter than its average magnitude.

Blazars show long-term variability across the electromagnetic spectrum from radio to gamma. The optical flux variability can be explained by several intrinsic scenarios and should be studied together with the color and spectral behavior, and the periodicity. The precession of the jet can cause LTV in the observed flux (Kudryavtseva et al. 2011). Since the emission mechanism remains the same, no change in the color behavior is expected and a (quasi)periodicity can coexist. The inhomogeneity of the jet, and instability of the accretion rate are other mechanisms of LTV.

4.2. Spectral Variability

We employed a simple power law in the form of $\log(F_\nu) = -\alpha \log(\nu) + C$ to obtain the nightly spectral indices (F is the flux density, ν is the frequency, and α is the spectral index). The results of the fits are shown in Table 5. The spectral

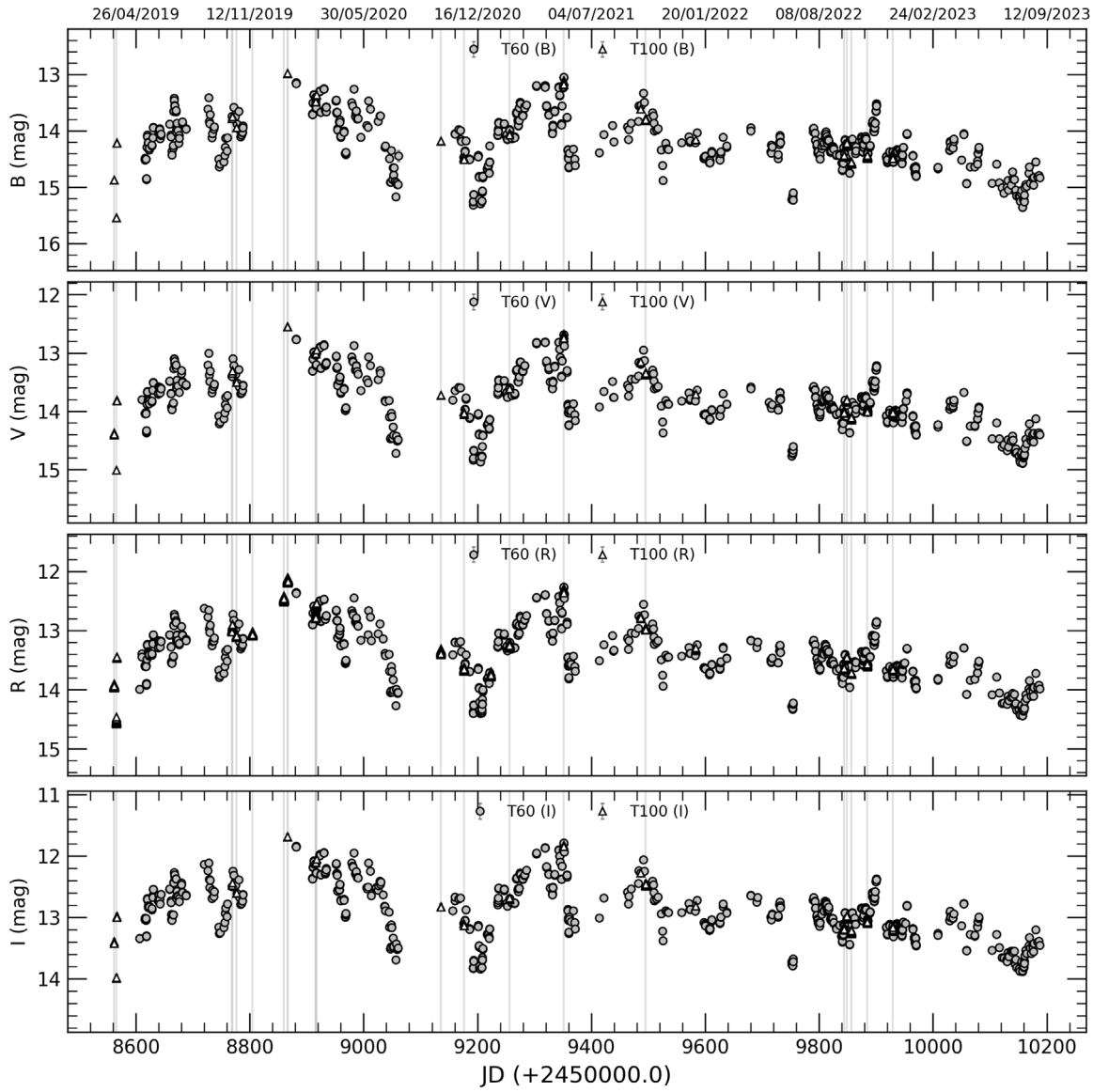

Figure 4. Long-term LCs of the blazar S5 0716+714 in the optical *B*, *V*, *R*, and *I* bands. Vertical lines represent the date of intraday observations as given in Figure 5.

Table 4
Results of the LTV Analysis of the Blazar S5 0716+714

Band	Brightest Magnitude/MJD	Faintest Magnitude/MJD	Average Magnitude	Variability Amplitude (%)
B	$12.979 \pm 0.010/58866.42621$	$15.540 \pm 0.016/58565.33069$	14.234 ± 0.015	256.123
V	$12.542 \pm 0.020/58866.42378$	$15.013 \pm 0.023/58565.32583$	13.821 ± 0.022	247.084
R	$12.109 \pm 0.011/58866.54426$	$14.580 \pm 0.013/58565.33793$	13.080 ± 0.012	247.043
I	$11.687 \pm 0.050/58866.42851$	$13.990 \pm 0.051/58565.32040$	12.910 ± 0.051	230.217

index varies between 0.828 and 1.432 during our observation period and the mean spectral index is 1.092. These results are similar to the study of Raiteri et al. (2021) in which it varies from 0.95 to 1.34 (mean value of 1.14).

To investigate the spectral behavior of the blazar S5 0716 +714, we studied the variation of the spectral index with time and *R*-band magnitude. We fitted a straight line to the plots of the spectral index (Figure 5) resulting in a slope of 0.06 with $r = 0.272$ and $p = 1.93\text{e-}07$. There is an aggregation of alpha between 13 and 14 mag when the brightness is in the medium state and the BWB behavior is also clearly visible in the plot.

We performed linear regression analysis on the spectral colors versus the *R*-mag of the long-term LC (Figure 6) to reveal the color behavior of the source. The slope values and the constants derived from these fits are listed in Table 6. Both Figure 5 and Figure 6 show that the object has a BWB behavior as can be seen in Table 6. The value of the B–I color index varies between 1.161 and 1.553 (mean value 1.337) during the

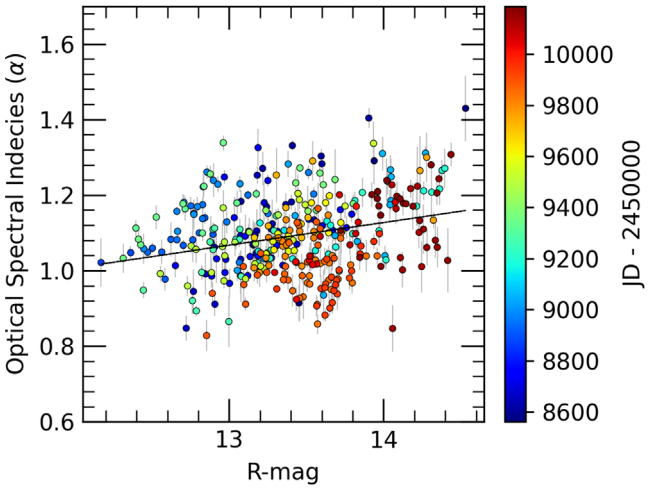

Figure 5. Optical spectral indices vs. *R*-mag plot of long-term observations in optical *BVRI* bands.

monitoring period. The variation in this value may be due to changes in the contribution of different emission components (Agarwal et al. 2016). As the object becomes brighter, the jet emission dominates the emission more from the central components and the host galaxy, so it becomes bluer.

4.3. Cross-correlation Analysis

In AGN studies, the detection of any time lag between different bands (and the scale of lag, if present) provides important clues to the emission region. For this purpose, the discrete correlation function (DCF) is a convenient statistical tool that can be applied to unevenly distributed time series (Agarwal & Gupta 2015, and references therein).

The DCF between two discrete data sets (a_i and b_j) can be computed using the unbinned DCF (UDCF) defined as follows:

$$\mathrm{UDCF}_{ij}(\tau) = \frac{(a_i - \bar{a})(b_j - \bar{b})}{\sqrt{(\sigma_a^2 - e_a^2)(\sigma_b^2 - e_b^2)}}, \quad (7)$$

where $\bar{a}$ and $\bar{b}$ represent the mean values of the two time-series data sets, and $\sigma_{a,b}$ and $e_{a,b}$ are their standard deviations and errors, respectively. $\Delta t_{ij} = (t_{bj} - t_{ai})$ indicates the time delay between the two data points. To obtain the DCF, the UDCF values are averaged over the interval $\tau - \frac{\Delta\tau}{2} \leqslant \tau_{ij} \leqslant \tau + \frac{\Delta\tau}{2}$ as described in the study by Edelson & Krolik (1988),

$$\mathrm{DCF}(\tau) = \frac{\sum_{k=1}^{m} \mathrm{UDCF}_k}{M}. \quad (8)$$

The quantity "*M*" represents the count of pairwise time lag values situated within the specified τ interval.

For the long-term LCs, we took the weighted mean magnitudes and the mean Julian Date (JD) of the nightly binned intranight observations. DCF analysis was applied to each pair combination of the optical *BVRI* bands for the long-term LCs (Figure 7). There is a strong correlation between all the bands and no time lag was detected considering a time binning value τ of 1 day, indicating that the source of the emission is cospatial.

Table 5
Straight Line Fits to Optical SEDs of the Blazar S5 0716+714

Date	α	C	r	p
2019-03-18	$+1.291 \pm 0.061$	-6.141 ± 0.903	+0.998	2.256e-03
2019-03-22	$+1.429 \pm 0.086$	-4.348 ± 1.269	+0.997	3.628e-03
2019-03-23	$+0.914 \pm 0.048$	-11.459 ± 0.699	+0.997	2.690e-03
...	...	...	...	...
...	...	...	...	...
2023-08-27	$+1.209 \pm 0.006$	-7.334 ± 0.087	+1.000	2.412e-05
2023-08-29	$+1.201 \pm 0.032$	-7.443 ± 0.472	+0.999	7.120e-04
2023-08-31	$+1.147 \pm 0.028$	-8.265 ± 0.411	+0.999	5.934e-04

Note. α = spectral index and C = intercept of $\log(F_\nu)$ against $\log(\nu)$; r = Correlation coefficient; p = null hypothesis probability.

(This table is available in its entirety in machine-readable form in the online article.)

4.4. Periodicity Search

In order to identify any periodicity on the LC, the LCs were analyzed using two widely used techniques: WWZ (Foster 1996) and LSP (Lomb 1976; Scargle 1982).

The LSP is a powerful tool used for detecting periodicity in the time series, which can provide clues for interpreting the structure of the central engine. Since the data points in our data set are not evenly distributed, the peaks can be interpreted as quasiperiodic signals in the corresponding time axis.

Although LSP is capable of detecting any periodic pattern in the time series, variations in AGN LCs do not follow a linear groove and they may have more than one periodicity and/or quasiperiodicity. The WWZ is a method for detecting such oscillations in the LC.

The results of the WWZ and LSP analysis are shown in Figure 8. Using the method[6] described in O'Neill et al. (2022), we have simulated 10,000 LCs corresponding to the power spectral density of the blazar LC. We then used WWZ and LSP to search for periodicity on the simulated LCs, as we had done on the blazar LC. The significance levels obtained are 95% and 99% for each frequency, which are shown with a red color in the plots. In the LSP plot, 188 and 530 days are found within 95% significance in the *R*-band LC. In the WWZ analysis, 186 ± 30 and 532 ± 76 days (within 99% significance) are found in the *R*-band LC. The results of these analyses in the *BVI* bands are very similar to those in the *R* band.

5. Discussion and Conclusions

During our observational campaign between 2019 March and 2023 August, the blazar was observed quasi-simultaneously for 416 nights in the optical *BVRI* bands with two optical telescopes, i.e., 1.0 m telescope and 0.6 m robotic telescope in Türkiye in both active and quiescent states The brightness of the source varied between 12.109 and 14.580 mag in the optical *R* band. In the long-term LC, the blazar had a variability amplitude of 256.123%, 247.084%, 247.043%, and 230.217% in the *BVRI* bands, respectively. To understand the underlying mechanism of the variability, the flux variability should be analyzed together with the color behavior. The blazar did not show a strong color change in the long-term LCs, and the emission in the *BVRI* bands was strongly correlated without any time lag, which can be interpreted as the source of the

[6] https://github.com/skiehl/lcsim

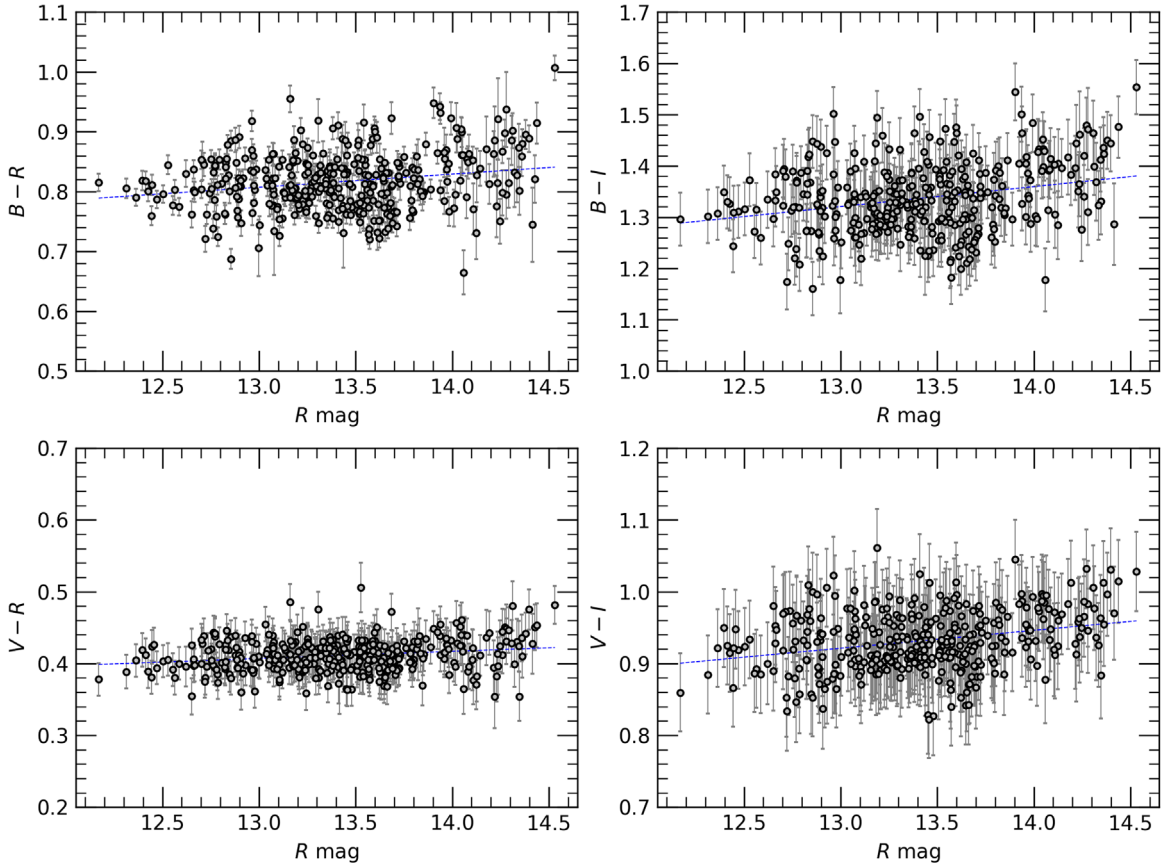

Figure 6. Color indices of long-term LCs.

Table 6
The Fit Result of LTV of the Spectral Indices and Color Behaviors

Model	Slope	Intercept	*r*-value	*p*-value
Time (JD) versus alpha	−4.3e-5 ± 1.1e-5	+107.746 ± +26.937	−0.206	9.086e-05
R-mag versus alpha	+0.060 ± 0.011	+0.288 ± +0.152	+0.272	1.934e-07
R-mag versus *B-R*	+0.022 ± 0.005	+0.522 ± +0.071	+0.212	4.045e-05
R-mag versus *B-I*	+0.039 ± 0.007	+0.814 ± +0.099	+0.269	2.270e-07
R-mag versus *V-R*	+0.010 ± 0.002	+0.279 ± +0.032	+0.205	5.107e-05
R-mag versus *V-I*	+0.025 ± 0.004	+0.597 ± +0.059	+0.282	3.105e-08

emission in these bands being cospatial. As the spectral window of the *BVRI* bands is very narrow compared to the entire electromagnetic spectrum of the blazars, it is more difficult to detect any in-correlation. Assuming that the flux comes from a nonthermal radiative process, we have generated nightly spectral indices by fitting a simple power law to the flux in the *BVRI* bands. The spectral index varies between 0.828 and 1.432 in the long-term LC. When the daily spectral indices are plotted against the *R*-band magnitude, α becomes steeper as the blazar becomes more active, so to speak, a slight BWB trend can be seen in the spectral energy distributions of the *BVRI* bands. In addition to the long-term variability, STVs (weeks and months timescale) are clearly visible in the long-term LC.

During the monitoring period, we observed the blazar for at least 1 hr in the optical *R* band on 21 nights, including six quasi-simultaneous observations in the *BVRI* bands. Statistical tests show that on 12 out of 21 nights, the blazar had a significant IDV with a magnitude change of ≈0.1 mag and a variability amplitude between 4.41 and 11.23 in the *BVRI* bands. The variability amplitude of the IDV LCs did not change significantly with the state. We have plotted the color–magnitude plots of six nights where the *BVRI* band observations are quasi-simultaneous. Although there are slight slopes in some colors, we cannot claim that there is a clear trend that varies with magnitude on the daily timescale.

To obtain the minimum timescale, we applied SF to the nightly *R*-band LCs that have the most significant variability. We found a minimum variability timescale of ∼48 minutes on the LC of 2021 February 10, from which we have calculated the minimum size of the emission region to be $\approx 10^{15}$ cm and the mass of the SMBH to be $5.69 \times 10^8\ M_\odot$ confirming the result of Kaur et al. (2018).

We employed different statistical techniques to detect potential (quasi)periodicity on the long-term LCs. The WWZ analysis showed that the blazar has quasiperiodicities of 186 ± 30 and 532 ± 76 days (within 99% significance) in the optical *R*-band LC. The LSP analyses give values close to those of the WWZ results, but the significance of the 586 days QPO falls between 95% and 99% levels. According to our simulations, the peak in the LSP graph at the ∼586 day period

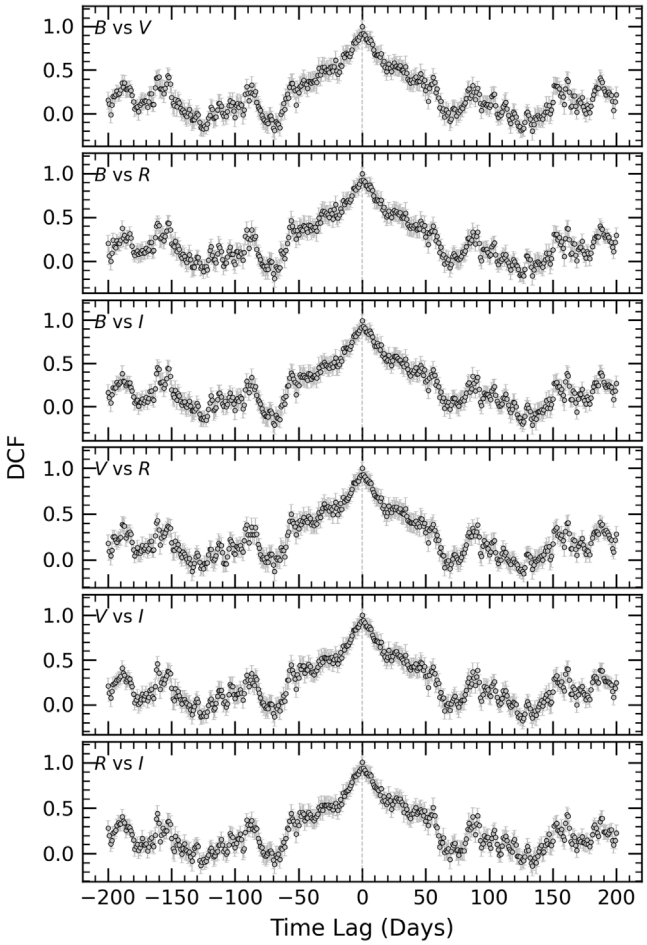

Figure 7. Cross-correlation analysis for *B*, *V*, *R*, and *I* bands using discrete correlation function for the entire monitoring period.

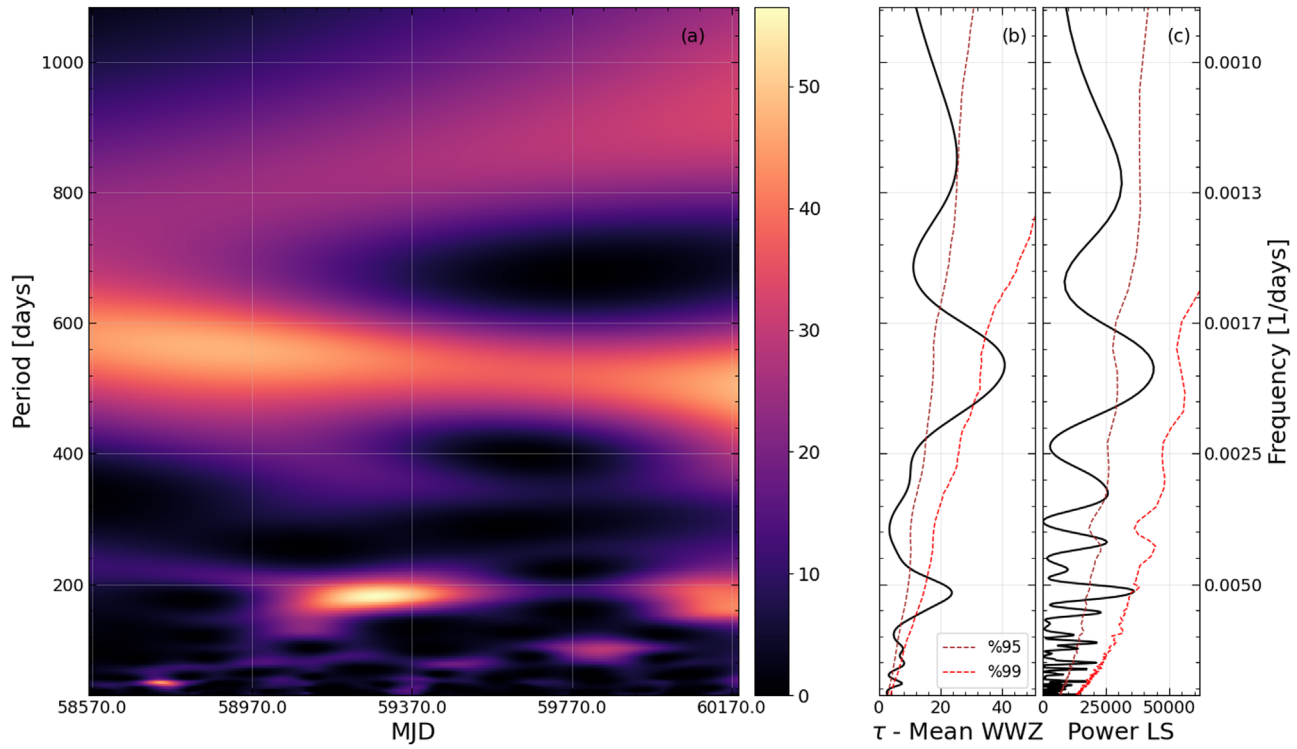

Figure 8. Graphs of the WWZ and LSP analysis of the long-term optical *R*-band LC. (a) WWZ power spectrum. (b) Plot of the WWZ analysis. (c) Plot of the LSP analysis.

is not significant considering the stochastic process. Although we found a similar peak at 523 days in the WWZ analyses, we cannot claim that this is a reliable QPO, as both analyses would be expected to show a significant peak. We interpret the 186 day QPO in the WWZ power spectrum as a local pattern indicating two outbursts in 2021 May and 2021 October. We did not detect any other QPO within the limits of significance, confirming the other results of the previous studies mentioned in Section 1.

Since the contribution from the host galaxy is negligible as a constant component (Gorbachev et al. 2022), it can be assumed that the source of the flux is mainly jet, and hence also the variability. The reason for the long-term variability is suggested by Rani et al. (2013) as geometrical effects. Lister et al. (2013) showed that S5 0716+714 has a jet with a changing position angle and can have a helical shape, which leads to a change in the Doppler factor. The change in the Doppler factor can cause both short- and long-term variability and can explain the quasi-chromatic variability of the emission.

Another model for the variability is shocks propagating through the jet (Blandford & Königl 1979; Marscher & Gear 1985). According to this model, changes in both the flux and color behavior can be caused by relativistic shocks propagating through a jet, and these shocks can interact with different emitting regions with different magnetic and particle compositions (Bhatta et al. 2013). The variability is interpreted together with the color behavior. The mild color change in the long-term variability and the unpredictable color behavior of the intraday and short-term variability support this model, as the shock front can encounter any such composition in the jet structure. If the emission component is strongly chromatic, it will influence the continuum's color (Agarwal & Gupta 2015). The occasional change in the color behavior can be a result of the inhomogeneity of the plasma both at the base and through the jet. Magnetic reconnection is a mechanism that explains fast variability, namely flares. When the opposing magnetic field lines join and change the magnetic composition, remarkable energy following a power law can be released, as this energy can also be optical (Zhang et al. 2022). The contribution of this process can be considered together with the polarization data. While the source is in the quiescent state, instabilities in the accretion disk, such as hotspots or changes in the accretion rate, can contaminate the LC and cause short-term variability.

The variability of the blazars is not fully understood. Further simultaneous multiwavelength and multimessenger observations together with the theoretical studies would greatly help to fully understand the astrophysical nature of these objects.

Acknowledgments

We thank TUBITAK National Observatory for partial support in using the T60 and T100 telescopes with project numbers 19BT60-1505 and 19AT100-1486, respectively. E.E. was supported, in part, by the Scientific Research Project Coordination Unit of Istanbul University (Project ID FDK-2022-39145). This study was supported by Scientific and Technological Research Council of Türkiye (TUBITAK) under the grant No. 121F427.

Data Availability

The data underlying this article are available (Figure 1; Tables 1 and 5).

Software: Astropy (Astropy Collaboration et al. 2013, 2018, 2022), ccdproc (Craig et al. 2017), Numpy (Harris et al. 2020), Matplotlib (Hunter 2007), Photutils (Bradley et al. 2020), WWZ (Kiehlmann et al. 2023), lcsim (Kiehlmann 2023).

ORCID iDs

Ergün Ege https://orcid.org/0000-0001-5778-5679
Aykut Özdönmez https://orcid.org/0000-0003-1399-5804
Aditi Agarwal https://orcid.org/0000-0003-4682-5166
Tansel Ak https://orcid.org/0000-0002-0688-1983

References

Abdo, A. A., Ackermann, M., Agudo, I., et al. 2010, ApJ, 716, 30
Abramowicz, M. A., & Nobili, L. 1982, Natur, 300, 506
Agarwal, A., & Gupta, A. C. 2015, MNRAS, 450, 541
Agarwal, A., Pandey, A., Özdönmez, A., et al. 2022, ApJ, 933, 42
Agarwal, A., Gupta, A. C., Bachev, R., et al. 2016, MNRAS, 455, 680
Anderhub, H., Antonelli, L. A., Antoranz, P., et al. 2009, ApJL, 704, L129
Astropy Collaboration, Robitaille, T. P., Tollerud, E. J., et al. 2013, A&A, 558, A33
Astropy Collaboration, Price-Whelan, A. M., Sipőcz, B. M., et al. 2018, AJ, 156, 123
Astropy Collaboration, Price-Whelan, A. M., Lim, P. L., et al. 2022, ApJ, 935, 167
Bessell, M. S., Castelli, F., & Plez, B. 1998, A&A, 333, 231
Bhatta, G., Webb, J. R., Hollingsworth, H., et al. 2013, A&A, 558, A92
Bhatta, G., Stawarz, Ł., Ostrowski, M., et al. 2016, ApJ, 831, 92
Blandford, R. D., & Königl, A. 1979, ApJ, 232, 34
Bradley, L., Sipőcz, B., Robitaille, T., et al. 2020, astropy/photutils: v1.0.1, Zenodo, doi:10.5281/zenodo.4049061
Carrasco, L., Escobedo, G., Recillas, E., et al. 2019, ATel, 13359, 1
Chandra, S., Baliyan, K. S., Ganesh, S., & Joshi, U. C. 2011, ApJ, 731, 118
Chandra, S., Zhang, H., Kushwaha, P., et al. 2015, ApJ, 809, 130
Chatterjee, R., Roychowdhury, A., Chandra, S., & Sinha, A. 2018, ApJL, 859, L21
Chen, J., Yi, T., Gong, Y., et al. 2022, ApJ, 938, 8
Craig, M., Crawford, S., Seifert, M., et al. 2017, astropy/ccdproc: v1.3.0.post1, Zenodo, doi:10.5281/zenodo.1069648
Dai, B.-z., Zeng, W., Jiang, Z.-j., et al. 2015, ApJS, 218, 18
de Diego, J. A. 2014, AJ, 148, 93
de Diego, J. A., Polednikova, J., Bongiovanni, A., et al. 2015, AJ, 150, 44
Edelson, R. A., & Krolik, J. H. 1988, ApJ, 333, 646
Elliot, J. L., & Shapiro, S. L. 1974, ApJL, 192, L3
Fan, J. H., Yang, J. H., Liu, Y., et al. 2016, ApJS, 226, 20
Foster, G. 1996, AJ, 112, 1709
Gallo, L. C., Blue, D. M., Grupe, D., Komossa, S., & Wilkins, D. R. 2018, MNRAS, 478, 2557
Gaur, H., Gupta, A. C., Bachev, R., et al. 2015, MNRAS, 452, 4263
Ghisellini, G., Villata, M., Raiteri, C. M., et al. 1997, A&A, 327, 61
Gorbachev, M. A., Butuzova, M. S., Sergeev, S. G., Nazarov, S. V., & Zhovtan, A. V. 2022, ApJ, 928, 86
Gupta, A. C., Fan, J. H., Bai, J. M., & Wagner, S. J. 2008a, AJ, 135, 1384
Gupta, A. C., & Joshi, U. C. 2005, A&A, 440, 855
Gupta, A. C., Cha, S.-M., Lee, S., et al. 2008b, AJ, 136, 2359
Gupta, A. C., Krichbaum, T. P., Wiita, P. J., et al. 2012, MNRAS, 425, 1357
Haiyan, Y., Xiefei, S., Xiaopan, L., et al. 2023, Ap&SS, 368, 88
Harris, C. R., Millman, K. J., van der Walt, S. J., et al. 2020, Natur, 585, 357
Heidt, J., & Wagner, S. J. 1996, A&A, 305, 42
Hong, S., Xiong, D., & Bai, J. 2017, AJ, 154, 42
Hong, S., Xiong, D., & Bai, J. 2018, AJ, 155, 31
Hunter, J. D. 2007, CSE, 9, 90
Kaur, N., Baliyan, K. S., Chandra, S., Sameer, & Ganesh, S. 2018, AJ, 156, 36
Kiehlmann, S., 2023 lcsim: Light curve simulation code, Astrophysics Source Code Library, ascl:2310.002
Kiehlmann, S., Max-Moerbeck, W., & King, O., 2023 wwz: Weighted wavelet z-transform code, Astrophysics Source Code Library, ascl:2310.003
Krawczynski, H. 2004, NewAR, 48, 367
Kudryavtseva, N. A., Britzen, S., Witzel, A., et al. 2011, A&A, 526, A51
Kuehr, H., Pauliny-Toth, I. I. K., Witzel, A., & Schmidt, J. 1981, AJ, 86, 854
Li, X.-P., Yang, H.-Y., Cai, Y., et al. 2023, ApJ, 943, 157
Liao, N. H., Bai, J. M., Liu, H. T., et al. 2014, ApJ, 783, 83
Lister, M. L., Aller, M. F., Aller, H. D., et al. 2013, AJ, 146, 120
Lomb, N. R. 1976, Ap&SS, 39, 447
Marscher, A. P., & Gear, W. K. 1985, ApJ, 298, 114

Marscher, A. P., & Travis, J. P. 1996, A&AS, 120, 537
Massaro, E., Mantovani, F., Fanti, R., et al. 2001, A&A, 374, 435
Montgomery, D. C. 2012, Design and Analysis of Experiments (8th ed.; Hoboken, NJ: Wiley)
O'Neill, S., Kiehlmann, S., Readhead, A. C. S., et al. 2022, ApJL, 926, L35
Ostorero, L., Wagner, S. J., Gracia, J., et al. 2006, A&A, 451, 797
Otero-Santos, J., Acosta-Pulido, J. A., Becerra González, J., et al. 2020, MNRAS, 492, 5524
Pandey, A., Gupta, A. C., Wiita, P. J., & Tiwari, S. N. 2019, ApJ, 871, 192
Pichel, A., Donzelli, C., Muriel, H., et al. 2023, A&A, 680, A52
Polednikova, J., Ederoclite, A., de Diego, J. A., et al. 2016, MNRAS, 460, 3950
Raiteri, C. M., Villata, M., Tosti, G., et al. 2003, A&A, 402, 151
Raiteri, C. M., Villata, M., Acosta-Pulido, J. A., et al. 2017, Natur, 552, 374
Raiteri, C. M., Villata, M., Carosati, D., et al. 2021, MNRAS, 501, 1100
Rani, B., Gupta, A. C., Strigachev, A., et al. 2010, MNRAS, 404, 1992
Rani, B., Krichbaum, T. P., Fuhrmann, L., et al. 2013, A&A, 552, A11
Romero, G. E., Boettcher, M., Markoff, S., & Tavecchio, F. 2017, SSRv, 207, 5
Romero, G. E., Cellone, S. A., & Combi, J. A. 1999, A&AS, 135, 477
Scargle, J. D. 1982, ApJ, 263, 835
Schlafly, E. F., & Finkbeiner, D. P. 2011, ApJ, 737, 103
Schmidt, K. B., Rix, H.-W., Shields, J. C., et al. 2011, ApJ, 744, 147
Simonetti, J. H., Cordes, J. M., & Heeschen, D. S. 1985, ApJ, 296, 46
Stalin, C. S., Gopal-Krishna, Sagar, R., et al. 2006, MNRAS, 366, 1337
Tripathi, T., Gupta, A. C., Takey, A., et al. 2024, MNRAS, 527, 5220
Urry, C. M., & Padovani, P. 1995, PASP, 107, 803
Villata, M., Raiteri, C. M., Lanteri, L., Sobrito, G., & Cavallone, M. 1998, A&AS, 130, 305
Villata, M., Raiteri, C. M., Kurtanidze, O. M., et al. 2002, A&A, 390, 407
Villata, M., Raiteri, C. M., Larionov, V. M., et al. 2008, A&A, 481, L79
Volvach, A. E., Volvach, L. N., Bychkova, V. S., et al. 2012, ARep, 56, 275
Wagner, S. J., & Witzel, A. 1995, ARA&A, 33, 163
Wagner, S. J., Witzel, A., Heidt, J., et al. 1996, AJ, 111, 2187
Wiita, P. J. 1996, in ASP Conf. Ser. 110, Blazar Continuum Variability, ed. H. R. Miller, J. R. Webb, & J. C. Noble (San Francisco, CA: ASP), 42
Yuan, Y.-H., Fan, J.-h., Tao, J., et al. 2017, A&A, 605, A43
Zhang, H., Li, X., Giannios, D., et al. 2022, ApJ, 924, 90